SANS: Publicly Available Daily Multi-Scale Seismic Ambient Noise Source Maps

Jonas Karl Hans Igel[1], Daniel C. Bowden[2], and Andreas Fichtner[1]

[1]ETH Zurich
[2]ETH Zürich

November 21, 2022

Abstract

Seismic ambient noise sources have received increased attention recently, creating new possibilities to study the Earth's subsurface and the atmosphere-ocean-solid Earth coupling. In efforts to locate such noise sources using nonlinear finite-frequency inversions, methodological developments such as pre-computed wavefields and spatially variable grids were necessary. These make inversions feasible for the secondary microseismic sources in a frequency range up to 0.2 Hz on a daily basis. By obtaining a starting model for the inversion using Matched Field Processing (MFP) we are able to further steer the inversion towards acceptable global noise source models and improve the final result. Analysis of one year of daily inversions shows the seasonal variations of the secondary microseisms and their dependence on the atmosphere-ocean-solid Earth coupling due to storm-induced ocean waves. We present a web framework, SANS (Seismic Ambient Noise Sources, sans.ethz.ch), where daily regional- to global-scale seismic ambient noise source maps are made available to the public. This eases the implementation of time-variable noise source distributions into full-waveform ambient noise tomography and time-dependent subsurface monitoring methods. Additionally, it encourages other studies to verify if changes in the seismic data are due to changes in the subsurface velocity or spatio-temporal variations of noise sources.

SANS: Publicly Available Daily Multi-Scale Seismic Ambient Noise Source Maps

Jonas K. H. Igel[1], Daniel C. Bowden[1], Andreas Fichtner [1]

[1]Institute of Geophysics, Department of Earth Sciences, ETH Zürich

Key Points:

- We combine Matched Field Processing and nonlinear finite-frequency inversion to locate ambient noise sources
- We present a web framework for publicly available daily regional to global scale seismic ambient noise source maps (`sans.ethz.ch`)
- Analysis of a full year of daily inversions shows the seasonal variations of the secondary microseisms

Corresponding author: Jonas K. H. Igel, `jonas.igel@erdw.ethz.ch`

Abstract

Seismic ambient noise sources have received increased attention recently, creating new possibilities to study the Earth's subsurface and the atmosphere-ocean-solid Earth coupling. In efforts to locate such noise sources using nonlinear finite-frequency inversions, methodological developments such as pre-computed wavefields and spatially variable grids were necessary. These make inversions feasible for the secondary microseismic sources in a frequency range up to 0.2 Hz on a daily basis. By obtaining a starting model for the inversion using Matched Field Processing (MFP) we are able to further steer the inversion towards acceptable global noise source models and improve the final result. Analysis of one year of daily inversions shows the seasonal variations of the secondary microseisms and their dependence on the atmosphere-ocean-solid Earth coupling due to storm-induced ocean waves. We present a web framework, SANS (Seismic Ambient Noise Sources, `sans.ethz.ch`), where daily regional- to global-scale seismic ambient noise source maps are made available to the public. This eases the implementation of time-variable noise source distributions into full-waveform ambient noise tomography and time-dependent subsurface monitoring methods. Additionally, it encourages other studies to verify if changes in the seismic data are due to changes in the subsurface velocity or spatio-temporal variations of noise sources.

Plain Language Summary

The Earth is constantly vibrating due to various man-made and natural sources. One of the main sources of natural background noise is the ocean, specifically when ocean waves come into contact with the solid Earth. The strength of these sources strongly depends on the wave height, which changes constantly due to atmospheric phenomena such as storms. We study these seismic waves, so-called seismic ambient noise, to analyse the spatial and temporal variations which allow us to study the interaction between the atmosphere, ocean, and solid Earth, as well as imaging the subsurface. In this study, we combine two different methods, namely Matched Field Processing (MFP) and nonlinear finite-frequency inversions, to create regional to global scale seismic ambient noise source maps on a daily basis. By looking at a full year of daily noise source maps we can observe the seasonal variations of noise sources. These daily noise source maps are presented on a website (`sans.ethz.ch`) where anyone can download the results and implement them in their own research. We hope that this will aid others by simplifying the implementation of noise source information which should make tomography and monitoring methods more accurate.

1 Introduction

Seismic ambient noise sources have been studied thoroughly over the last few decades. Specifically, since studies showed that they could be used to study the Earth's interior (Aki, 1957; Shapiro & Campillo, 2004; Shapiro et al., 2005; Sabra et al., 2005) further research was performed to understand the generation of ambient vibrations (e.g. Ardhuin, Stutzmann, et al., 2011; Ardhuin & Herbers, 2013; Ardhuin et al., 2015; Gualtieri et al., 2014, 2015), and new methods were developed to help locate these sources (e.g. Gerstoft & Tanimoto, 2007; Retailleau et al., 2017; Retailleau & Gualtieri, 2019; Gal et al., 2018; Sager, Ermert, et al., 2018; Ermert et al., 2020; Igel et al., 2021). More data-driven methods like correlation-based beamforming have been used to obtain the directionality (e.g. Bucker, 1979; Hinich, 1979; Ruigrok et al., 2017) and physical location (e.g. Ishii et al., 2005; Meng et al., 2012; Retailleau et al., 2017; Retailleau & Gualtieri, 2019) of noise sources.

In theory, cross-correlation functions approach the Green's functions for homogeneously distributed, uncorrelated, random noise sources and an equipartioned wavefield.

Many ambient noise interferometry studies assume that the noise sources are sufficiently homogeneous for the cross-correlations to converge to Green's functions (e.g. Nakata et al., 2019; Snieder & Wapenaar, 2010; Weaver et al., 2009; Wapenaar, 2004; Wapenaar & Fokkema, 2006). However, several studies have shown that the omni-present ambient noise wavefield changes on a daily basis (e.g. Bertelli, 1872; Longuet-Higgins, 1950; Ardhuin et al., 2015) and the cross-correlation and Green's function diverge if more realistic constraints - such as global or local energy and directionality constraints - are implemented into the modelling (Tsai & Sager, 2022). The heterogeneity of noise source distributions can have a significant effect on travel times, particularly for monitoring applications (Zhan et al., 2013; Delaney et al., 2017). Prior knowledge of the noise source locations can help distinguish if changes in the cross-correlations are due to changes in the noise source distribution or subsurface velocities.

Inspired by work in helioseismology (Woodard, 1997), recent works introduced the direct numerical modelling of noise cross-correlations for any heterogeneous noise source distribution on Earth (Tromp et al., 2010; Hanasoge, 2013b; Fichtner, 2014; Ermert et al., 2017; Sager, Ermert, et al., 2018; Datta et al., 2019). This has resulted in several studies using adjoint techniques (e.g. Fichtner et al., 2006) and sensitivity kernels (e.g. Tromp et al., 2010; Fichtner, 2014) to invert for the seismic ambient noise source distribution for different frequency ranges on various scales (Ermert et al., 2017; Xu et al., 2019; Igel et al., 2021). Expanding on these adjoint and sensitivity kernel techniques, Bowden et al. (2021) showed that certain beamforming algorithms are mathematically similar to the first iteration of nonlinear finite-frequency inversions.

The direct forward-modelling of ambient noise cross-correlations allows us to circumvent common assumptions in ambient noise studies - e.g. wavefield equipartitioning and a quasi-random noise source distribution - that are necessary for Green's function retrieval (e.g. Shapiro & Campillo, 2004; Shapiro et al., 2005; Wapenaar & Fokkema, 2006; Sánchez-Sesma & Campillo, 2006). Additionally, full-waveform ambient noise tomography methods are capable of directly implementing information about the noise source distribution (Sager, Ermert, et al., 2018). Recent developments have made the computation of cross-correlations for ambient noise source inversions more efficient by using spatially variable grids and pre-computed Green's function databases (Ermert et al., 2020; Igel et al., 2021); particularly for the frequency range of secondary microseismic sources (between 0.1 and 0.2 Hz). This allows us to rapidly invert for the noise source distribution on a regional to global scale with reasonable computational cost by taking advantage of high performance computing (HPC) resources.

Building on these various developments, we present a web framework to make daily Seismic Ambient Noise Source (SANS) maps available to the public (`sans.ethz.ch`). In-depth knowledge of the ambient noise source distribution should help to improve ambient noise tomography and imaging methods; particularly to ensure that changes in the subsurface are not confused with the spatio-temporal variations of the microseismic noise source distribution. Providing these maps should ease the implementation in full waveform ambient noise tomography methods and encourage future studies to take the noise source distribution into account.

In this paper, we focus on the combination of Matched Field Processing (MFP) with nonlinear finite-frequency inversions to improve the inversion results, and present the web framework SANS, where the daily ambient noise maps are made publicly available. Since both methods have previously been described individually in detail, we refer the interested reader to earlier publications for more in-depth derivations and explanations (Bowden et al., 2021; Ermert et al., 2020; Igel et al., 2021).

2 Methodology

In the following section, we will explain the main steps of the two methods: nonlinear finite-frequency inversions and Matched Field Processing (MFP). Despite the differences in the approaches taken, Bowden et al. (2021) show that these methods are well connected. Both have their advantages and disadvantages: MFP is an efficient, data-driven approach that works on any cross-correlation data. An inversion is computationally more expensive but - in contrast to MFP - models the wave propagation more accurately and allows us to account for the nonlinearity by using an iterative approach.

More importantly, an inversion allows for prior knowledge to be implemented. Hence we use the more efficient, data-driven MFP algorithm to compute a starting model for the nonlinear finite-frequency inversion, to avoid local minima and accelerate the convergence towards an acceptable model. Both methods rely on the fact that vertical-component seismic ambient noise data in the frequency range of 0.1 to 0.2 Hz are dominated by surface waves.

2.1 Nonlinear Finite-Frequency Inversion

The inversion method is based on a concept from helioseismology (Woodard, 1997) which enables the direct modelling of cross-correlations for any noise source power-spectral density (PSD). The work has been adapted for applications to Earth by several authors (e.g. Tromp et al., 2010; Hanasoge, 2013a; Fichtner, 2014; Ermert et al., 2017; Sager, Ermert, et al., 2018) with some additional implementations of pre-computed wavefields (Ermert et al., 2020) and spatially variable grids (Igel et al., 2021) to improve efficiency and make inversions feasible for higher frequencies. In the following section we will provide a short overview of the gradient-based iterative inversion method. For more details, the reader is referred to the aforementioned publications.

2.1.1 Cross-correlation modelling

The following equation allows us to forward model the cross-correlation wavefield $\mathcal{C}_{ij}$, for two stations at locations $\boldsymbol{x}_1$ and $\boldsymbol{x}_2$, for an arbitrary noise source PSD S_{nm}, at points $\boldsymbol{\xi}$ on the Earth's surface $\partial\oplus$, using the Green's functions $\boldsymbol{G}$, in the frequency domain (Fichtner, 2014; Ermert et al., 2017; Sager, Boehm, et al., 2018; Igel et al., 2021):

$$\mathcal{C}_{ij}(\boldsymbol{x}_1, \boldsymbol{x}_2) = \int\limits_{\partial\oplus} G^*_{in}(\boldsymbol{x}_1, \boldsymbol{\xi}) G_{jm}(\boldsymbol{x}_2, \boldsymbol{\xi}) S_{nm}(\boldsymbol{\xi}) d\boldsymbol{\xi}. \tag{1}$$

We imply the Einstein summation convention for repeated indices, and * indicates the complex conjugate. To reduce the computational cost we pre-compute the Green's functions $\boldsymbol{G}$ using the time-domain spectral-element codes for spherically symmetric Earth models AxiSEM to model wave propagation (Nissen-Meyer et al., 2014), and Instaseis to extract seismograms (van Driel et al., 2015) with 1-D isotropic PREM (Dziewonski & Anderson, 1981) as underlying velocity model. The Green's function database is then re-used for subsequent iterations and inversions. Additionally, we implement spatially variable grids with regional dense areas and no grid points on land, to reduce the number of possible noise sources, and thus the modelling parameters for regional applications (Igel et al., 2021). The combination of pre-computed wavefields and spatially variable grids allows us to efficiently invert for the noise source distribution of the secondary microseisms in a frequency range of 0.1 to 0.2 Hz (Ermert et al., 2020; Igel et al., 2021).

2.1.2 Inversion

Once we have modelled the synthetic cross-correlations, we measure the difference to the observed cross-correlations using the logarithmic energy ratio (e.g. Ermert et al.,

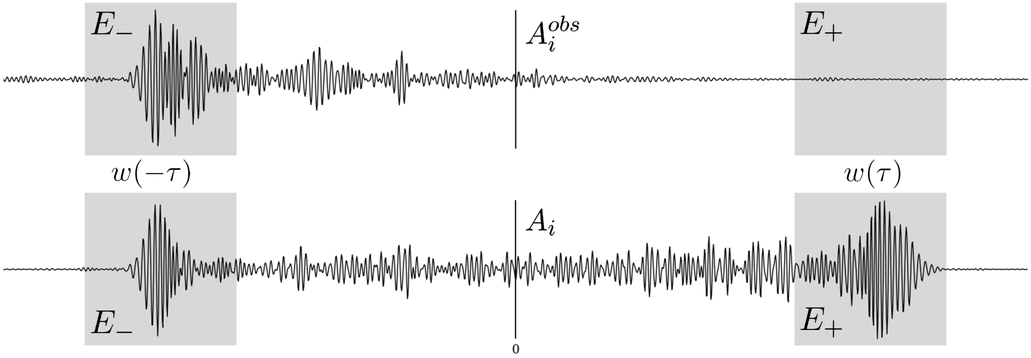

Figure 1. Our chosen measurement is the logarithmic energy ratio as previously used by Ermert et al. (2020) and Igel et al. (2021) (see Equation 2). To obtain a misfit we take a measurement of synthetic A_i (bottom) and observed A_i^{obs} (top) cross-correlations and compute the L_2-norm (see Equation 3).

2017). This measurement quantifies the asymmetry of the cross-correlation which arises from a heterogeneous noise source distribution as illustrated in Figure 1. The logarithmic energy ratio computes the ratio of the energies E_+ and E_- of the expected surface wave arrival window $w(\tau)$ in the causal and acausal parts of the cross-correlation $C(\tau)$:

$$A = \ln\left(\frac{\int [w(\tau)C(\tau)]^2 d\tau}{\int [w(-\tau)C(\tau)]^2 d\tau}\right) = \ln\left(\frac{E_+}{E_-}\right) \tag{2}$$

In contrast to full-waveform misfits, the logarithmic energy ratio aims to match the energy in the causal and acasual expected surface wave arrival windows. Although this measurement contains less information, it is much more robust, and relatively insensitive to unknown 3-D Earth structure (Sager, Boehm, et al., 2018) due to only comparing energies in a certain time window. Consequently, this allows us to use a simple 1-D PREM (Dziewonski & Anderson, 1981) velocity model to compute synthetic cross-correlations. During the inversion we aim to minimise the squared L_2-norm, i.e. the misfit χ, of the measurements A_i and A_i^{obs} on the synthetic and observed cross-correlations, respectively:

$$\chi = \frac{1}{2}\sum_{i=1}^{N}\left[A_i - A_i^{obs}\right]^2 \tag{3}$$

where N is the number of measurements.

Adjoint techniques (e.g. Fichtner et al., 2006) allow us to compute source sensitivity kernels (e.g. Tromp et al., 2010; Hanasoge, 2013b; Fichtner, 2014) which provide a spatial reference of where an increase or decrease in noise source strength should decrease the misfit. By compiling the gradient, i.e. the sum of all sensitivity kernels, we can update the noise source distribution and continue with the next iteration by re-computing the cross-correlations, misfits, and sensitivity kernels. To minimise the misfit we adopt a gradient-based iterative scheme using the steepest descent method, including regularisation and step-length tests. Several synthetic and real-data tests have shown that there are usually no significant improvements in the noise source distribution after roughly 5 iterations. Hence, we run 8 iterations of the inversion to ensure that we have converged to a model that explains the data based on our measurement.

In previous research (Igel et al., 2021), we used a homogeneous distribution in the ocean as the initial noise source distribution. For a gradient-based iterative inversion method like ours, a good initial model can be helpful in steering the inversion towards an acceptable global noise source model and avoid local minima.

By introducing a different method to locate noise sources - namely Matched Field Processing - we are able to efficiently create a more realistic initial model from the same observed cross-correlations. This is similar to full-waveform inversions, where starting models are often constructed with more efficient methods such as ray-based travel time tomography or dispersion curve analysis (e.g. Virieux & Operto, 2009; Teodor et al., 2021).

2.2 Matched Field Processing

Matched Field Processing, in this context, may be considered similar to beamforming and backprojection methods, where time-shifts are applied to the data and rays are backprojected to obtain a source location. However, whereas beamforming generally assumes plane waves arrive at an array of sensors, MFP directly considers sources anywhere within a computational domain and estimates travel times accordingly. This makes it very suitable for global ambient noise source studies, where stations from all over the globe may be used. Additionally, it is able to map noise sources on any grid, which allows us to use the same source grid for MFP and the inversion.

MFP algorithms of varying complexity have been developed, for example: to locate hydrothermal acoustic sources (Cros et al., 2011); microseismic sources in exploration geophysics (Corciulo et al., 2012); glacial tremors (Umlauft et al., 2021); or applied to three-component seismic array data for microseisms (Gal et al., 2018). The algorithm could also be adapted to be nearly identical to full-waveform methods by including synthetic Green's functions (Bowden et al., 2021; Schippkus & Hadziioannou, 2022). Although there may be some value to more complex MFP implementations, we prefer the computationally efficient version described below, as the subsequent inversion iterations will add further complexity.

2.2.1 Constant Velocity MFP

Our MFP algorithm is based on the assumption that a point source at a proposed noise source location for a set surface wave group velocity will lead to signal in the cross-correlation at a certain lag. The first step is to compute all cross-correlations and create a grid of possible noise sources. Subsequently, we iterate over all possible noise sources and compute the travel times to the stations based on a constant surface wave speed v of 2,900 $\frac{m}{s}$. This surface wave speed is roughly the average Rayleigh wave group velocity in the 0.1 to 0.2 Hz frequency range in PREM (Dziewonski & Anderson, 1981) and has provided good results for synthetic and real-data applications. For such a narrow frequency band we can consider the group velocity to be roughly constant. The travel time difference Δt_{ij} between arrivals t_i and t_j at the two receiver locations $\boldsymbol{x_i}$ and $\boldsymbol{x_j}$ determines the lag at which the current noise source location $\boldsymbol{x}$ would result in a signal in the cross-correlation:

$$\Delta t_{ij} = t_i - t_j = \frac{||\boldsymbol{x} - \boldsymbol{x_i}||}{v} - \frac{||\boldsymbol{x} - \boldsymbol{x_j}||}{v}. \tag{4}$$

Note that $||.||$ denotes the vector norm for a 2-D example as illustrated in Figure 2. For our applications we extend the vector norm from 2-D to a sphere where it is adapted to be the great circle distance between the noise source locations and stations.

Finally, the corresponding value of the cross-correlation - or in our case the value of the square envelope of the cross-correlation as explained in section 2.2.2 - is added to the 'power' of that grid point, and we repeat the process for the next possible noise source location. This is equivalent to applying phase shifts to the raw signals and then measuring coherencies, as MFP or beamforming is often described. An illustration of this

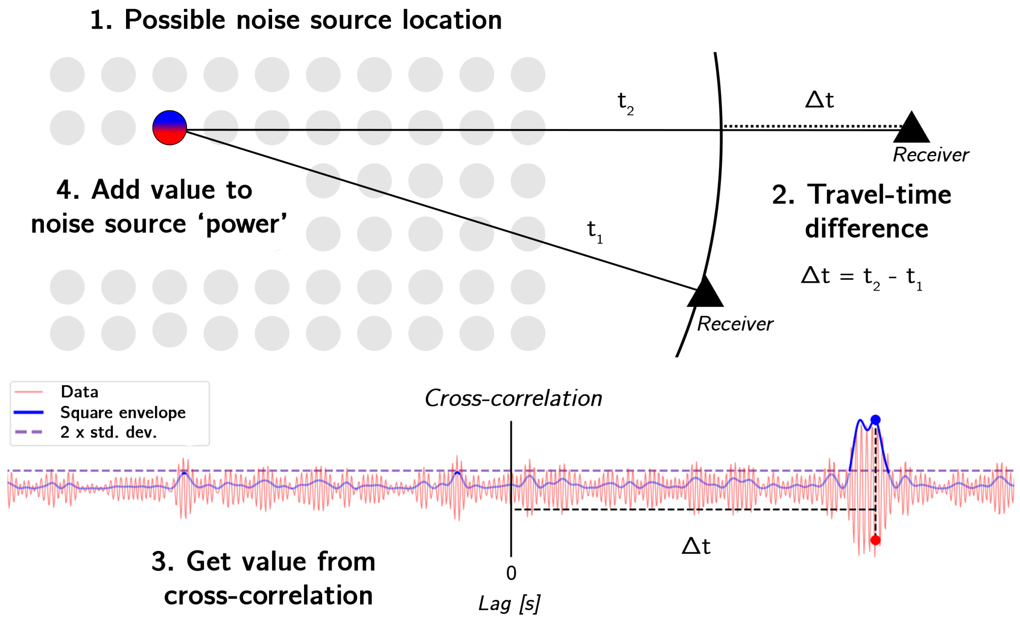

Figure 2. Illustration of the Matched Field Processing algorithm. We iterate over all possible noise sources, calculate the travel time difference Δt and finally obtain the value from the cross-correlation, e.g. red dot for the actual waveform value or blue dot for the value of the square envelope. Additionally, we calculate the standard deviation of the envelope and set everything below twice the standard deviation to 0. This increases the signal-to-noise ratio and improves the final MFP power map. This process is repeated for every possible noise source location and every station pair.

algorithm can be seen in Figure 2. By using a larger array of stations, we are able to spatially restrict the locations of noise sources and obtain a map of noise source 'power'.

2.2.2 Square Envelope Measurement

The simplest MFP method uses the value of the cross-correlation waveform to obtain the 'power' for each noise source location. However, since this often results in strong fluctuations of the noise source power due to the oscillatory nature of the waveforms and struggles with low signal-to-noise ratios we instead take the value of the square envelope $S(C(\tau))$ of the cross-correlation $C(\tau)$.

$$S(C(\tau)) = C^2(\tau) + \mathcal{H}(C(\tau))^2, \tag{5}$$

where $\mathcal{H}$ indicates the Hilbert transform. Additionally, we compute the standard deviation $\sigma(S(C(\tau)))$ of the square envelope and set all values below twice the standard deviation to 0, i.e. we do not add any 'power' for those noise source locations.

Besides increasing the signal-to-noise ratio when a signal is present, this also smooths the resulting noise source and avoids the fluctuations of noise source power. This does mean that for cross-correlations with no clear signal, i.e. where the square envelope is nearly constant, nothing is removed and the signal-to-noise ratio can not be increased. This has little effect on the final MFP power distribution as it would add a near constant value.

$$P(C(\tau_i)) = \begin{cases} 0 & \text{if } S(C(\tau_i)) < 2 * \sigma(S(C(\tau))) \\ S(C(\tau_i)) & \text{else}\,, \end{cases} \tag{6}$$

where $P(C(\tau_i))$ is the MFP power for the time lag τ at source location i and cross-correlation $C(\tau_i)$. Synthetic and real data tests show that using the square envelope with a cut-off threshold greatly increases the contrast of the final MFP maps and ensures that we mainly use the signal from the cross-correlations.

To account for geometric spreading we multiply each value of the square envelope of the cross-correlations with an amplitude decay factor D_i as introduced by previous studies (e.g. Corciulo et al., 2012; Bowden et al., 2021), which depends on the surface wave group velocity v, the average frequency of our bandpass filter f, and the average distance of the station pair to the proposed source location r_i:

$$D_i = \sqrt{\frac{2v}{\pi f r_i}} \tag{7}$$

This process is repeated for all possible noise source locations and cross-correlations, and the values of the square envelope of the cross-correlations are added up as illustrated in Figure 2. Of course, more sophisticated methods to model either the travel times or amplitude decays and attenuation can be implemented in MFP (Bowden et al., 2021; Schippkus & Hadziioannou, 2022). Such modelling is precisely the point of subsequent iterations of the full-waveform approach, whereas the MFP is only intended to give a computationally efficient initial model.

In contrast to other array-based beamforming methods, MFP works best when the stations surround the noise source location. We illustrate this in Figure 3 by running a synthetic example, where we forward model cross-correlations using the pre-computed Green's function database and cross-correlation model code from the inversion with a dominant noise source blob within the domain, and a frequency content of 0.1 to 0.2 Hz. We apply the MFP algorithm to two sets of stations: 6 stations in closer proximity and 35 stations spread out in the whole domain. If the dominant noise source is outside the array we see strong smearing and MFP is only able to give us a direction of the dominant noise source. On the other hand, if the dominant noise source is surrounded by stations, MFP is able to constrain the spatial extent of the dominant noise sources more accurately.

2.3 MFP starting model

Thanks to MFP being most capable when the dominant noise sources are within the array, it is a useful method to locate noise sources on a regional to global scale. MFP and the finite-frequency inversion use slightly different information from the cross-correlation to obtain a noise source distribution. The logarithmic energy ratio is largely insensitive to unknown Earth structure, as it only takes the energy in a given window but ignores the actual waveform. On the other hand, MFP with the square envelope measurement uses more information from the waveform itself but does not properly account for wave propagation. Additionally, the resulting MFP maps are harder to interpret in terms of physical units as they are not an actual model of a physical quantity but rather an image of the noise source distribution.

To combine the two methods we normalise a smoothed MFP noise source map and set it as the initial power-spectral density model for the finite-frequency inversion. In con-

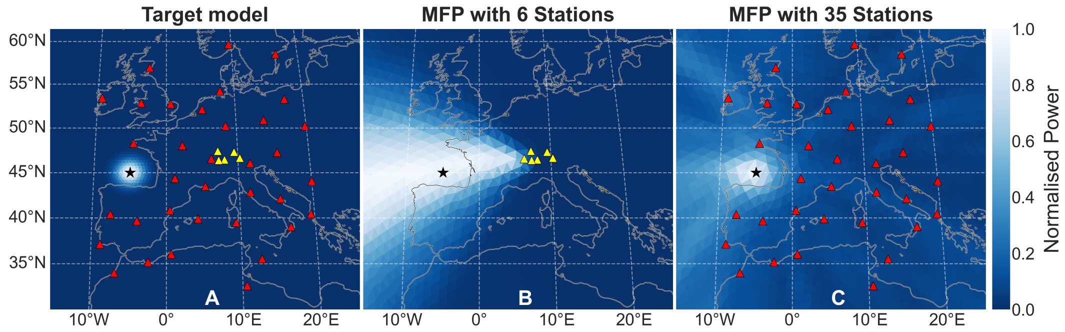

Figure 3. Example of the MFP algorithm for synthetic cross-correlations modelled with a dominant noise source blob (⋆) within the domain (A). If the dominant noise source is outside the array (▲), MFP is mainly able to provide a direction (B). If the stations surround the dominant noise source (▲), MFP is able to constrain the spatial extent of the dominant noise source much more accurately (C).

trast to the previously used homogeneous starting model, this greatly reduces the presence of inversion artefacts. Synthetic and real-data tests have shown that this improves the final noise source maps without significantly increasing the computational cost. Figure 4 shows a regional synthetic comparison of two inversions with a homogeneous and an MFP starting model. The synthetic cross-correlations were modelled using the noise source distribution on the left with added random noise to make them more realistic. The random noise is introduced by normalising a random time series, multiplying it by the maximum amplitude of the cross-correlation and a scaling factor of 1.5, and finally adding it to the cross-correlation. Comparisons show that this resembles our real ambient noise cross-correlations more closely.

The inversion with the homogeneous starting model does contain the most dominant noise sources but shows a strong tendency to move noise sources closer to the coast, especially for the large dominant noise source area off the European coast. In contrast, the inversion with an MFP starting model does not lead to strong coastal sources, and better represents the spatial distribution of the dominant noise sources in the actual model. This is particularly useful for global inversions where MFP can help to avoid inversion artefacts due to lack of data by increasing the probability of noise sources in certain areas before the first iteration.

MFP introduces new information to the inversion, as it actually uses the cross-correlation waveforms, as opposed to the finite-frequency inversion where we measure the energy in the expected surface wave arrival time windows. Hence, we expect this to reduce the null space of the inversion and produce a more accurate noise source map. Despite the clear differences in the resulting inversion models, the misfits of the final iterations shown in Figure 4 are very similar. However, it is clear that the inversion with the MFP starting model is visually more similar to the target model than the inversion with a homogeneous starting model. This indicates that including the additional waveform information via the MFP starting model does reduce the null space and helps to steer the inversion in a direction that is more closely aligned with the actual noise source distribution.

3 SANS: Daily Seismic Ambient Noise Sources

In light of the recent developments that have significantly decreased the computational cost of ambient noise source inversions for the secondary microseisms on a global scale (Ermert et al., 2020; Igel et al., 2021), we introduce a new web framework, SANS,

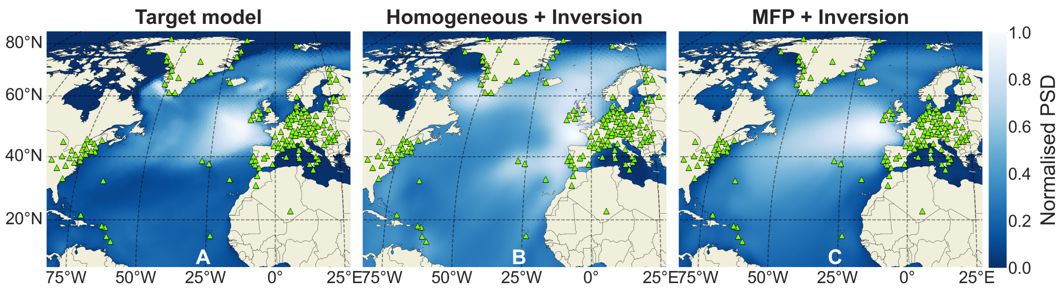

Figure 4. Synthetic inversions using cross-correlations with added random noise that were forward-modelled with the noise source distribution on the left (A) for stations surrounding the North Atlantic (▲). A homogeneous starting model introduces stronger noise sources along the coast during the inversion (B). In contrast, an inversion with an MFP starting model results in a noise source distribution that is closer to the target model (C).

where daily Seismic Ambient Noise Sources are made available to the public (`sans.ethz.ch`). Currently, we run two inversions every day: one for a global station list and one more regional with stations surrounding the North Atlantic. A regional inversion allows for a higher spatial resolution of the noise source distribution in that area.

Users can obtain the inversion results by either directly looking at a plot of the noise source distribution maps online or downloading the inversion output and analysing it themselves, e.g. for implementation in other studies.

3.1 Data selection and processing

We download and process the seismic ambient noise data automatically every morning at 4 am (CET) using ObsPy (Krischer et al., 2015). All stations within a chosen station list are checked for available data. The station lists are based on globally available broadband sensors but limit the minimum distance between stations to roughly 1° (= 111 km) to avoid smaller arrays. Dense station arrays would lead to high local sensitivities that would distort the final noise source distribution. This results in 414 stations for the global and 153 stations for the North Atlantic station list. The global distribution of stations is illustrated in the resolution analysis in Figure 5 and both station lists can be downloaded from the website. The data availability changes on a daily basis, leading to roughly 70% of these stations having data available on average.

After downloading all available data, we remove the instrument response, downsample to 1 Hz, segment the data into 2 h windows, and remove any windows containing earthquakes that are in the GCMT catalogue (Ekström et al., 2012) with a minimum magnitude of 5.6. Occasionally this can lead to all windows being removed if there was one strong or several smaller earthquakes in a day. Subsequently, we compute the daily cross-correlations of the windowed seismic ambient noise data by stacking the individual cross-correlations of the 12 windows. This helps to increase the signal-to-noise ratio of the final daily ambient noise cross-correlations.

Similar to Igel et al. (2021), we ignore cross-correlations with a signal-to-noise ratio below 3.5. The signal-to-noise ratio is determined by dividing the maximum amplitude within the expected surface wave arrival window by the standard deviation of the whole time series. Hence, we define a signal as a clear surface wave arrival within the expected window. This is usually the case if the dominant noise source is in-line with the station pair. Due to our chosen measurement being the logarithmic energy ratio, cross-correlations with little signal - i.e. asymmetry - would not contribute much to the final gradient and update of the noise source distribution. Besides improving the final result of the inversion, ignoring cross-correlations below a signal-to-noise threshold also decreases the computational cost, as fewer cross-correlations have to be modelled during the inversion. During the inversion we apply a band-pass filter between 0.1 and 0.2 Hz as we focus on the secondary microseismic noise sources.

3.2 Web framework

After the data have been downloaded, processed, and correlated we run 8 iterations of the inversion on Piz Daint, a supercomputer at the Swiss National Supercomputing Centre (CSCS). The computational cost of the inversions varies with the number of available cross-correlations for each day. However, we greatly reduce the computational cost since we have already pre-computed the wavefield and extracted the Green's function database which is re-used every day. We run both inversions, one global and one regional surrounding the North Atlantic, on 600 cores, with the usual computational times being 60 minutes (50 node hours) and 30 minutes (25 node hours), respectively. We use two different spatially variable grids, with a more homogeneous distribution of about 29,000 grid points for the global inversion and a locally dense grid in the North Atlantic with roughly 21,000 grid points for the regional inversion. Once the inversions are done, we plot the output and copy all relevant files to the ETH web server where the website is hosted. These files are then made available to the public on `sans.ethz.ch`.

The web framework allows users to look through the iterations of all available inversion results and compare them to significant wave height maps (Tolman & Chalikov, 1996; *WAVEWATCH III*, 2005) of that day. Note that the generation mechanism of the secondary microseisms requires ocean waves travelling in opposite directions to overlap (Nakata et al., 2019); therefore the wave height maps are merely a reference as to where the areas of dominant noise sources may be and should not be directly compared. Users can download the full inversion output folder including the parameter file, station list, source grid, further plots such as the gradients, misfit reduction and other relevant files. We provide code that helps a user to plot and analyse these results themselves. In theory, the inversions are reproducible as the inversion code is made available on github. However, this does require the additional computation or download of an AxiSEM wavefield and access to HPC facilities. The global inversion requires roughly 50 node hours which includes the data download, processing, and 8 iterations of the inversion but excludes the extraction of a Green's function database.

3.3 Resolution analysis

Recent efforts have estimated the resolution and covariance of noise source full waveform inversions by treating it as a linear problem and using singular value decomposition (Xu & Mikesell, 2022). However, due to our nonlinear measurement of the logarithmic energy ratio this is not applicable to our inversion method. To show the effect of the changing data and station availability on the resolution of the inversions, we forward model cross-correlations with added noise for 414 stations around the globe and perform inversions with different station lists in Figure 5. The noise source distribution that we use to forward-model the data is an adapted significant wave height map from the WaveWatch III model (Tolman & Chalikov, 1996; *WAVEWATCH III*, 2005). The inversions are run with the same parameters as the daily SANS inversions. We choose different station lists from daily inversions to give a realistic station distribution that would be used for real-data inversions.

The inversion with 414 stations shows the model that we are able to recover using all potential stations. Due to the much higher station density in the Northern Hemisphere the resolution is higher and we are able to recover the dominant noise sources more

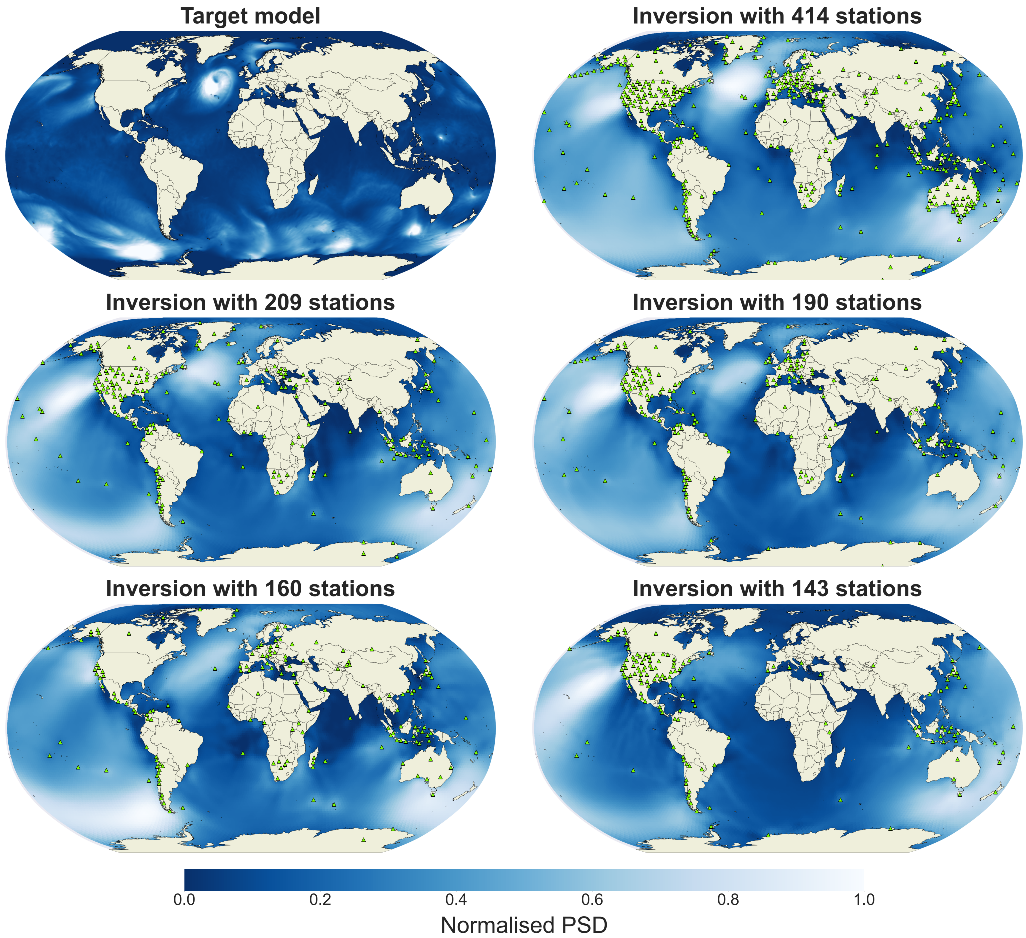

Figure 5. Synthetic inversions for the target model to show the effect of different stations (▲) on the final inversion models. Inversions with fewer stations still capture the most dominant noise sources in the final model.

accurately than in the Southern Hemisphere. As we decrease the number of stations we can see how the recovered model changes, especially when the stations are predominantly in Europe (160 stations) or North America (143 stations). However, even the inversions with fewer stations still include the most dominant noise sources from the target model. In that sense, the daily global inversions should not necessarily be seen as the global noise source distribution for each day, but rather the noise source distribution that the given station list is able to observe. Generally, the resolution in the Southern Hemisphere is lower due to the lack of station coverage and the North Atlantic usually has the highest resolution since it is surrounded by stations in Europe and North America.

3.4 Example applications

In the following section we present two example applications of the daily SANS maps. Firstly, we take the average of the daily inversions for Northern Hemisphere summer and winter to study the seasonal variations of the secondary microseisms. Secondly, we model cross-correlations for different noise source distribution models to illustrate the effect of a changing noise source distribution on the cross-correlation waveforms.

3.4.1 Seasonal analysis

Secondary microseismic sources are generated when two oceans travelling in opposite directions overlap, which in turn creates a vertical pressure wave. This induces seismic waves at the ocean bottom. The strength of these sources is directly related to the wave height of the overlapping waves (Longuet-Higgins, 1950; Hasselmann, 1963; Nakata et al., 2019; Ardhuin, Hanafin, et al., 2011).

Due to the seasonal variations in significant wave height we would expect a similar pattern for the noise source distribution of the secondary microseisms, which has already been observed over a century ago (Klotz, 1910; Burbank, 1912; Banerji, 1925). This relationship has recently been studied for various different frequency bands of microseisms ranging from the hum to secondary microseismic sources (Nishida & Fukao, 2007; Rhie & Romanowicz, 2006; Ermert et al., 2017; Stutzmann et al., 2012; Landés et al., 2010; Gualtieri et al., 2021). Thus, we would expect similar patterns to emerge if we average the daily inversions generated by the SANS workflow.

We include 335 daily inversions from the 17th May 2021 to the 2nd May 2022 in the analysis and choose to define Northern Hemisphere summer (21st April to 21st October) and winter (21st October to 21st April) based on the Icelandic first day of summer in 2022. The final iterations of all inversions within those two time ranges are averaged, resulting in 164 inversions for the summer and 171 for the winter months. Before averaging, we smooth the noise source model with a 4° Gaussian smoothing filter to avoid any artefacts from small changes in the inversion parameters during that time period.

Similarly, we average the significant wave height maps from the WaveWatch III model (Tolman & Chalikov, 1996) as a comparison. This should not be taken as a direct comparison but more as a reference of where the probability of more dominant noise sources is higher. The actual mechanism of generation of secondary microseismic sources is more complicated and requires more complex modelling (Ardhuin, Stutzmann, et al., 2011; Ardhuin & Herbers, 2013; Nakata et al., 2019). Figure 6 shows the comparison of the normalised average significant wave height with the normalised PSD of the average SANS inversions for Northern Hemisphere summer and winter.

The average inversions show clear seasonal variations that are in-line with our expectations. During the Northern Hemisphere summer the more dominant noise sources are in the Southern Hemisphere, specifically the South Pacific. As shown by previous studies on seasonal noise source variations (Landés et al., 2010; Gualtieri et al., 2021; Stutzmann et al., 2012), the Northern Hemisphere winter is dominated by noise sources in the North Atlantic. This supports the result of previous studies and shows that the SANS inversions are able to observe the spatio-temporal variations of the secondary microseismic sources on various timescales.

3.4.2 Cross-correlation modelling

A changing noise source distribution has a significant effect on the cross-correlations, particularly on a global scale. A common assumption is a homogeneous noise source distribution which, in theory, results in a symmetric cross-correlation. However, the noise source distribution is often strongly heterogeneous and changes constantly. We forward model cross-correlations using our modelling code from the inversion for three different noise source distributions to illustrate the changes: (i) homogeneous distribution everywhere, (ii) homogeneous distribution in the ocean, and (iii) the final SANS inversion model for the 9th March 2022.

In Figure 7 we plot the cross-correlations for 6 station pairs and the three different models. The cross-correlations are filtered between 0.1 and 0.2 Hz. As the noise source

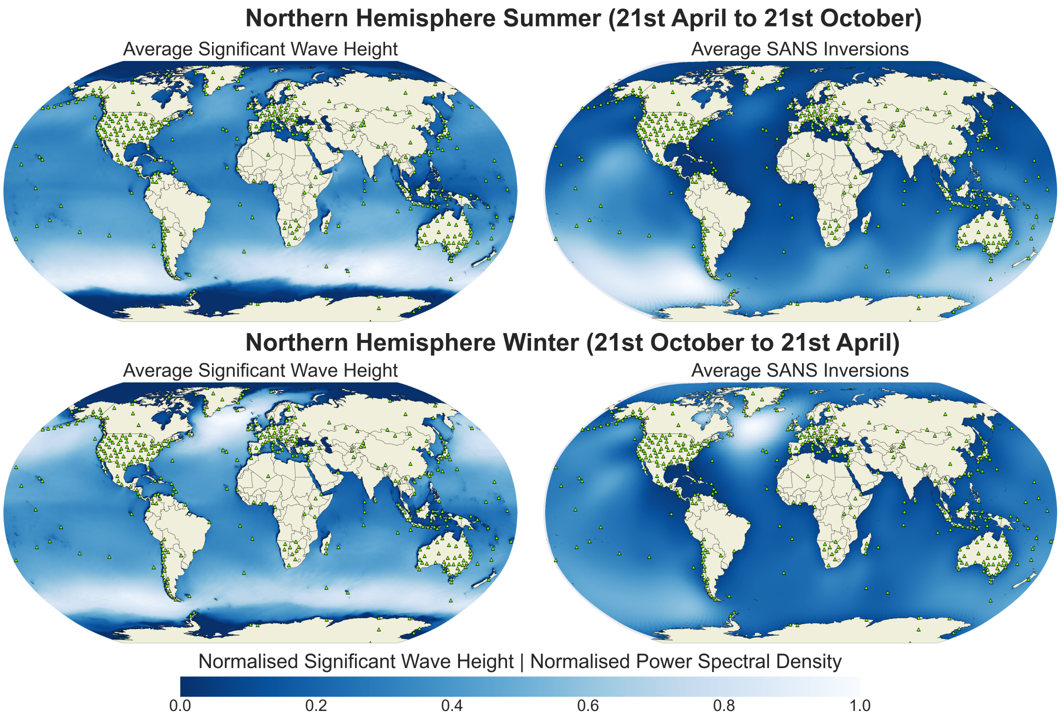

Figure 6. Comparison of the normalised average significant wave height and normalised PSD of the SANS daily inversion results for Northern Hemisphere summer (21st April to 21st Oct) and winter (21st Oct to 21st April) using a global station distribution (▲). Northern Hemisphere summer is dominated by sources in the Southern Hemisphere and Northern Hemisphere winter is dominated by sources in the North Atlantic.

distribution becomes more realistic, the changes to the cross-correlations become more and more significant. Especially for full waveform ambient noise studies, the influence of a changing noise source distribution should not be ignored. In many cases the main arrival also shifts significantly which makes travel time picking more difficult. We encourage future ambient noise studies to consider including information about the noise source distribution.

4 Discussion

With the daily computation of seismic ambient noise source maps we are able to study the interaction between the atmosphere, the ocean, and the solid Earth in near real-time. The daily maps show the clear heterogeneous nature of secondary microseismic noise sources and their strong spatio-temporal variations. Since the generation mechanism of secondary microseismic sources is quite well understood (Longuet-Higgins, 1950; Ardhuin, Stutzmann, et al., 2011; Ardhuin & Herbers, 2013; Ardhuin et al., 2015), these variations can also be studied by computing ocean surface pressure maps (Ardhuin, Stutzmann, et al., 2011) using significant wave height and bathymetry data. A comparison in our previous research (Igel et al., 2021) shows that these ocean surface pressure maps and finite-frequency inversions coincide quite well with similar areas of dominant noise sources present in both. Similarly, we observe correlation between the location of dominant noise sources in our daily SANS maps with respect to the higher amplitude significant wave heights. Due to the generation mechanism requiring two overlapping waves travelling in opposite directions, this comparison should only be considered as a rough reference of where there is a higher probability of dominant noise sources.

Particularly for ambient noise tomography and monitoring, knowledge of the noise source distribution is vital to circumvent common assumptions like the quasi-randomness of the noise field and equipartitioning of the wavefield. For these methods, daily maps can help reduce the misinterpretation of noise distribution changes as subsurface velocity changes. (Sager, Ermert, et al., 2018) inverted for both the noise source distribution and subsurface structure at the same time. However, this comes at an increased computational cost. By already having knowledge of the noise source distribution beforehand, we can reduce the complexity and computational cost of such full-waveform ambient noise tomography methods. As we illustrate in Figure 7, a heterogeneous noise source distribution can have a significant effect on the cross-correlations which should not be neglected, especially in full waveform ambient noise studies.

To make our inversion process as efficient as possible we use a simple 1-D PREM Earth model to simulate the Green's functions and cross-correlations. Despite (Sager, Boehm, et al., 2018) showing that our measurement of the logarithmic energy ratio is largely insensitivity to unknown 3-D Earth structure, this simplification could have an effect on the inversion. However, seismic studies within our frequency range of 0.1 to 0.2 Hz are generally considered less sensitive to small heterogeneities in the crust. Future studies might incorporate more complex Earth models (e.g. Fichtner et al., 2018) by precomputing the Green's function database using a wavefield solver like Salvus (Afanasiev et al., 2019). This would also allow the implementation of a fluid ocean layer and 3-D structure, albeit at the cost of increased computation time.

Furthermore, since the availability of ambient noise data changes daily, the number of stations included in the daily inversions can fluctuate greatly. This has an effect on the spatial sensitivity of the inversion, as dominant noise sources cannot be resolved without data from surrounding stations. In combination with the lack of grid points on land due to our parameterisation, this can lead to inversion artefacts in areas where we would not necessarily expect dominant noise sources; for example in marginal seas like Hudson Bay or the Mediterranean Sea. This also happens when there is a lack of coherent signals in the cross-correlations which are then ignored due to our data selection based

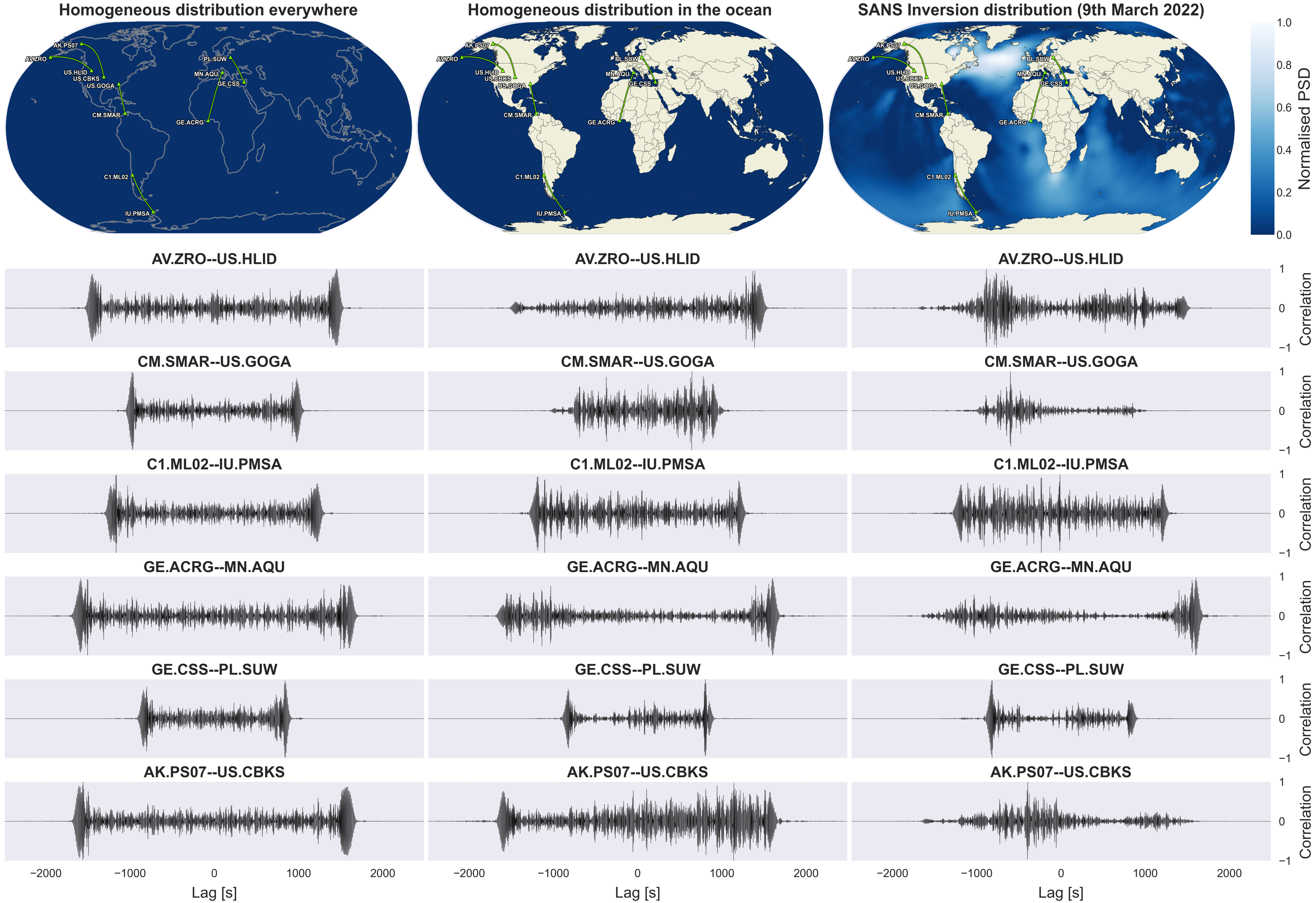

Figure 7. Comparison of modelled cross-correlations for 6 station pairs (▲) and three different noise source distributions: (i) homogeneous everywhere, (ii) homogeneous in the ocean, and (iii) final SANS inversion model for the 9th March 2022. As the noise source distribution becomes more realistic, the changes in the cross-correlations become more and more significant. This effect should not be ignored in ambient noise studies. Note that the noise source distribution for the homogeneous forward models are set to 1 everywhere, not 0 as indicated by the colourbar.

on the signal-to-noise ratio. To analyse the effect of the changing data and station availability on the resolution, we perform a synthetic test where we forward model cross-correlations with added noise and invert for them using different station lists. Generally, the inversions with fewer stations still include the most dominant noise sources, albeit with a lower spatial resolution.

5 Conclusions and Outlook

We present a new web framework SANS (`sans.ethz.ch`) where daily seismic ambient noise source maps for the secondary microseisms on a regional to global scale are made available to the public. Two methods are combined to improve the final noise source distribution: Matched Field Processing (MFP) and a gradient-based iterative finite-frequency inversion. The efficient data-driven MFP approach provides a starting model to steer the inversion in the right direction. Pre-computed wavefields and spatially variable grids have decreased the computational cost of the inversions, allowing us to run the inversions every morning for the previous days' data and presenting the results shortly after. Users are able to download the inversion results and we provide code to ease the implementation of the noise source distribution maps into other workflows. Comparisons to significant wave height maps do show that areas with high waves and strong dominant noise sources often coincide, which is in-line with the generation mechanism of secondary microseisms. Furthermore, we compute the averages of the noise sources maps for Northern Hemisphere summer and winter and compare them to the averages of the significant wave height maps. These show very similar areas of stronger activity which are in-line with other studies: Northern Hemisphere summer has more dominant sources in the Southern Hemisphere and Northern Hemisphere winter is dominated by noise sources in the North Atlantic.

We hope that making the noise source distribution data readily available to the public encourages new tomographic studies and methods exploiting seismic ambient noise vibrations. The accuracy of tomographic models could be improved by implementing knowledge of the noise sources. Specifically studies that make assumptions about a homogeneous or quasi-random noise source distribution would benefit and this may lead to more accurate velocity models. Studies that focus on time-dependent velocity changes in the subsurface often try to observe changes on the order of 1% or less (e.g. Zhan et al., 2013; Delaney et al., 2017). Particularly for such monitoring purposes, it is important to verify that these changes are not a result of a changing noise source distribution. The near real-time seismic ambient noise source maps we present here are a crucial tool to provide this verification. Future applications could also make this approach feasible for more local studies like the near real-time monitoring of avalanches and landslides.

Acronyms

CSCS Centro Svizzero di Calcolo Scientifico
ETH Eidgenössische Technische Hochschule Zürich
GCMT Global Centroid Moment Tensor
HPC High-Performance Computing
MFP Matched Field Processing
PREM Preliminary Reference Earth Model
PSD Power-Spectral Density
SANS Seismic Ambient Noise Sources

Data availability

The website introduced here can be found on `https://sans.ethz.ch/`. The inversion code is available on github: `https://github.com/jigel/noisi_inv` and is based on previous work (Ermert et al., 2020; Igel et al., 2021). Within the repository is a Jupyter Notebook Tutorial on how to run an inversion, including downloading, processing, and cross-correlating the data. Pre-computed AxiSEM wavefields that can be downloaded and implemented are available online at `http://ds.iris.edu/ds/products/syngine`.

The seismic data was collected from multiple data centers using ObsPy (Krischer et al., 2015) and the authors thank everyone involved in setting up and maintaining these: IRIS (http://service.iris.edu), GEOFON (http://geofon.gfz-potsdam.de), ORFEUS (http://www.orfeus-eu.org), NIEP (http://eida-sc3.infp.ro), RESIF (http://ws.resif.fr), INGV (http://webservices.ingv.it), SCEDC (http://service.scedc.caltech.edu), BGR (http://eida.bgr.de), ETH (http://eida.ethz.ch), KOERI (http://eida.koeri.boun.edu.tr), LMU (http://erde.geophysik.uni-muenchen.de), NCEDC (http://service.ncedc.org).

Acknowledgments

This work was supported by a grant from the Swiss National Supercomputing Centre (CSCS) under project ID s1040 and the help of their support team was much appreciated. Fruitful discussions with Dr. Sölvi Thrastarson, Krystyna Smolinski and other members of the SWP group at ETH Zürich helped improved this manuscript significantly.

References

Afanasiev, M., Boehm, C., van Driel, M., Krischer, L., Rietmann, M., May, D. A., … Fichtner, A. (2019). Modular and flexible spectral-element waveform modelling in two and three dimensions. *Geophysical Journal International*, *216*(3), 1675–1692. doi: 10.1093/gji/ggy469

Aki, K. (1957). Space and time spectra of stationary stochastic waves, with special reference to microtremors. *Bulletin of the Earthquake Research Institute*, *35*, 415–456. Retrieved from `https://ci.nii.ac.jp/naid/10003122622/en/`

Ardhuin, F., Gualtieri, L., & Stutzmann, E. (2015). How ocean waves rock the Earth: Two mechanisms explain microseisms with periods 3 to 300s. *Geophysical Research Letters*, *42*(3), 765–772. doi: 10.1002/2014GL062782

Ardhuin, F., Hanafin, J., Quilfen, Y., Chapron, B., Queffeulou, P., Obrebski, M., … Vandemark, D. (2011). Calibration of the IOWAGA global wave hindcast (1991–2011) using ECMWF and CFSR winds. *Proceedings of the 2011 International Workshop on Wave Hindcasting and Forecasting and 3rd Coastal Hazard Symposium, Kona, HI, USA.*, *30*.

Ardhuin, F., & Herbers, T. H. (2013). Noise generation in the solid Earth, oceans and atmosphere, from nonlinear interacting surface gravity waves in finite depth. *Journal of Fluid Mechanics*, *716*, 316–348. doi: 10.1017/jfm.2012.548

Ardhuin, F., Stutzmann, E., Schimmel, M., & Mangeney, A. (2011). Ocean wave sources of seismic noise. *Journal of Geophysical Research: Oceans*, *116*(C9), 1–21. doi: 10.1029/2011JC006952

Banerji, S. K. (1925, December). Microseisms and the Indian Monsoon. *Nature*, *116*(2928), 866–866. Retrieved 2022-05-11, from `https://www.nature.com/articles/116866b0` doi: 10.1038/116866b0

Bertelli, T. (1872). Osservazioni sui piccoli movimenti dei pendoli. *Bullettino Meteorologico dell'Osservatorio*, *XI*(11).

Bowden, D. C., Sager, K., Fichtner, A., & Chmiel, M. (2021). Connecting beamforming and kernel-based noise source inversion. *Geophysical Journal International*, *224*(3), 1607–1620. doi: 10.1093/gji/ggaa539

Bucker, H. P. (1979). High resolution cross-sensor beamforming for a billboard array.

Journal of the Acoustical Society of America, *65*(1), 145–147. doi: 10.1121/1.382256

Burbank, J. E. (1912, May). Microseisms caused by frost action. *American Journal of Science*, *33*, 474–475. Retrieved 2022-05-11, from https://ui.adsabs.harvard.edu/abs/1912AmJS...33..474B doi: 10.2475/ajs.s4-33.197.474

Corciulo, M., Roux, P., Campillo, M., Dubucq, D., & Kuperman, W. A. (2012). Multiscale matched-field processing for noise-source localization in exploration geophysics. *Geophysics*, *77*(5), KS33–KS41. doi: 10.1190/geo2011-0438.1

Cros, E., Roux, P., Vandemeulebrouck, J., & Kedar, S. (2011). Locating hydrothermal acoustic sources at Old Faithful Geyser using Matched Field Processing. *Geophysical Journal International*, *187*(1), 385–393. doi: 10.1111/j.1365-246X.2011.05147.x

Datta, A., Hanasoge, S., & Goudswaard, J. (2019). Finite-Frequency Inversion of Cross-Correlation Amplitudes for Ambient Noise Source Directivity Estimation. *Journal of Geophysical Research: Solid Earth*, *124*(7), 6653–6665. doi: 10.1029/2019JB017602

Delaney, E., Ermert, L., Sager, K., Kritski, A., Bussat, S., & Fichtner, A. (2017). Passive seismic monitoring with nonstationary noise sources. *Geophysics*, *82*(4), KS57–KS70. doi: 10.1190/GEO2016-0330.1

Dziewonski, A. M., & Anderson, D. L. (1981). Preliminary reference Earth model. *Physics of the earth and planetary interiors*, *25*(4), 297–356.

Ekström, G., Nettles, M., & Dziewoński, A. M. (2012, June). The global CMT project 2004–2010: Centroid-moment tensors for 13,017 earthquakes. *Physics of the Earth and Planetary Interiors*, *200-201*, 1–9. Retrieved 2022-05-11, from https://www.sciencedirect.com/science/article/pii/S0031920112000696 doi: 10.1016/j.pepi.2012.04.002

Ermert, L., Igel, J., Sager, K., Stutzmann, E., Nissen-Meyer, T., & Fichtner, A. (2020). noisi : A Python tool for ambient noise cross-correlation modeling and noise source inversion. *Solid Earth Discussions 2020*, 1 – 27. doi: 10.5194/se-11-1597-2020

Ermert, L., Sager, K., Afanasiev, M., Boehm, C., & Fichtner, A. (2017). Ambient Seismic Source Inversion in a Heterogeneous Earth: Theory and Application to the Earth's Hum. *Journal of Geophysical Research: Solid Earth*, *122*(11), 9184–9207. doi: 10.1002/2017JB014738

Fichtner, A. (2014). Source and processing effects on noise correlations. *Geophysical Journal International*, *197*(3), 1527–1531. doi: 10.1093/gji/ggu093

Fichtner, A., Bunge, H. P., & Igel, H. (2006). The adjoint method in seismology: II. Applications: traveltimes and sensitivity functionals. *Physics of the Earth and Planetary Interiors*, *157*(1-2), 105–123.

Fichtner, A., van Herwaarden, D.-P., Afanasiev, M., Simutė, S., Krischer, L., Çubuk Sabuncu, Y., … Igel, H. (2018). The Collaborative Seismic Earth Model: Generation 1. *Geophysical Research Letters*, *45*(9), 4007–4016. Retrieved 2022-05-11, from https://onlinelibrary.wiley.com/doi/abs/10.1029/2018GL077338 doi: 10.1029/2018GL077338

Gal, M., Reading, A. M., Rawlinson, N., & Schulte-Pelkum, V. (2018). Matched Field Processing of Three-Component Seismic Array Data Applied to Rayleigh and Love Microseisms. *Journal of Geophysical Research: Solid Earth*, *123*(8), 6871–6889. doi: 10.1029/2018JB015526

Gerstoft, P., & Tanimoto, T. (2007). A year of microseisms in southern California. *Geophysical Research Letters*, *34*(20). doi: 10.1029/2007GL031091

Gualtieri, L., Bachmann, E., Simons, F. J., & Tromp, J. (2021, July). Generation of secondary microseism Love waves: effects of bathymetry, 3-D structure and source seasonality. *Geophysical Journal International*, *226*(1), 192–219. Retrieved 2022-05-04, from https://doi.org/10.1093/gji/ggab095 doi: 10.1093/gji/ggab095

Gualtieri, L., Stutzmann, E., Capdeville, Y., Farra, V., Mangeney, A., & Morelli, A. (2015). On the shaping factors of the secondary microseismic wavefield. *Journal of Geophysical Research: Solid Earth*, *120*(9), 6241–6262. doi: 10.1002/2015JB012157

Gualtieri, L., Stutzmann, E., Farra, V., Capdeville, Y., Schimmel, M., Ardhuin, F., & Morelli, A. (2014). Modelling the ocean site effect on seismic noise body waves. *Geophysical Journal International*, *197*(2), 1096–1106. doi: 10.1093/gji/ggu042

Hanasoge, S. M. (2013a). The influence of noise sources on cross-correlation amplitudes. *Geophysical Journal International*, *192*(1), 295–309. doi: 10.1093/gji/ggs015

Hanasoge, S. M. (2013b). Measurements and kernels for source-structure inversions in noise tomography. *Geophysical Journal International*, *196*(2), 971–985. doi: 10.1093/gji/ggt411

Hasselmann, K. (1963). A statistical analysis of the generation of microseisms. *Reviews of Geophysics*, *1*(2), 177–210. doi: 10.1029/RG001i002p00177

Hinich, M. J. (1979). Maximum likelihood estimation of the position of a radiatina source in a waveauide. *Journal of the Acoustical Society of America*, *66*(2), 480–483. doi: 10.1121/1.383099

Igel, J. K. H., Ermert, L. A., & Fichtner, A. (2021). Rapid finite-frequency microseismic noise source inversion at regional to global scales. *Geophysical Journal International*, *227*(1), 169–183.

Ishii, M., Shearer, P. M., Houston, H., & Vidale, J. E. (2005). Extent, duration and speed of the 2004 Sumatra-Andaman earthquake imaged by the Hi-Net array. *Nature*, *435*(7044), 933–936. doi: 10.1038/nature03675

Klotz, O. (1910, August). Microseisms. *Science*. Retrieved 2022-05-11, from `https://www.science.org/doi/pdf/10.1126/science.32.816.252` doi: 10.1126/science.32.816.252

Krischer, L., Megies, T., Barsch, R., Beyreuther, M., Lecocq, T., Caudron, C., & Wassermann, J. (2015). ObsPy: A bridge for seismology into the scientific Python ecosystem. *Computational Science and Discovery*, *8*(1), 0–17. doi: 10.1088/1749-4699/8/1/014003

Landés, M., Hubans, F., Shapiro, N. M., Paul, A., & Campillo, M. (2010). Origin of deep ocean microseisms by using teleseismic body waves. *Journal of Geophysical Research: Solid Earth*, *115*(5), 1–14. doi: 10.1029/2009JB006918

Longuet-Higgins, M. S. (1950). A Theory of the Origin of Microseisms. *Philosophical Transactions of the Royal Society of London*, *243*(857), 1–35. doi: 10.1515/9783110242751.237

Meng, L., Ampuero, J. P., Stock, J., Duputel, Z., Luo, Y., & Tsai, V. C. (2012). Earthquake in a maze: Compressional rupture branching during the 2012 Mw 8.6 Sumatra earthquake. *Science*, *337*(6095), 724–726. doi: 10.1126/science.1224030

Nakata, N., Gualtieri, L., & Fichtner, A. (2019). *Seismic Ambient Noise*. Cambridge University Press. Retrieved from `https://books.google.ch/books?id=MWAkuwEACAAJ`

Nishida, K., & Fukao, Y. (2007). Source distribution of Earth's background free oscillations. *Journal of Geophysical Research: Solid Earth*, *112*(B6). doi: 10.1029/2006JB004720

Nissen-Meyer, T., Driel, M. v., Stähler, S. C., Hosseini, K., Hempel, S., Auer, L., ... Fournier, A. (2014). AxiSEM: broadband 3-D seismic wavefields in axisymmetric media. *Solid Earth*, *5*(1), 425–445. Retrieved from `https://www.solid-earth.net/5/425/2014/` doi: 10.5194/se-5-425-2014

Retailleau, L., Boué, P., Stehly, L., & Campillo, M. (2017). Locating Microseism Sources Using Spurious Arrivals in Intercontinental Noise Correlations. *Journal of Geophysical Research: Solid Earth*, *122*(10), 8107–8120. doi: 10.1002/

2017JB014593

Retailleau, L., & Gualtieri, L. (2019). Toward High-Resolution Period-Dependent Seismic Monitoring of Tropical Cyclones. *Geophysical Research Letters*, *46*(3), 1329–1337. doi: 10.1029/2018GL080785

Rhie, J., & Romanowicz, B. (2006). A study of the relation between ocean storms and the Earth's hum. *Geochemistry, Geophysics, Geosystems*, *7*(10). Retrieved 2022-05-04, from https://onlinelibrary.wiley.com/doi/abs/10.1029/2006GC001274 doi: 10.1029/2006GC001274

Ruigrok, E., Gibbons, S., & Wapenaar, K. (2017). Cross-correlation beamforming. *Journal of Seismology*, *21*(3), 495–508. doi: 10.1007/s10950-016-9612-6

Sabra, K. G., Gerstoft, P., Roux, P., Kuperman, W. A., & Fehler, M. C. (2005). Surface wave tomography from microseisms in Southern California. *Geophysical Research Letters*, *32*(14), 1–4. doi: 10.1029/2005GL023155

Sager, K., Boehm, C., Ermert, L., Krischer, L., & Fichtner, A. (2018). Sensitivity of Seismic Noise Correlation Functions to Global Noise Sources. *Journal of Geophysical Research: Solid Earth*, *123*(8), 6911–6921. doi: 10.1029/2018JB016042

Sager, K., Ermert, L., Boehm, C., & Fichtner, A. (2018). Towards full waveform ambient noise inversion. *Geophysical Journal International*, *212*(1), 566–590. doi: 10.1093/gji/ggx429

Schippkus, S., & Hadziioannou, C. (2022, March). *Matched Field processing for complex Earth structure* (Tech. Rep. No. EGU22-252). Copernicus Meetings. Retrieved 2022-06-20, from https://meetingorganizer.copernicus.org/EGU22/EGU22-252.html (Conference Name: EGU22) doi: 10.5194/egusphere-egu22-252

Shapiro, N. M., & Campillo, M. (2004). Emergence of broadband Rayleigh waves from correlations of the ambient seismic noise. *Geophysical Research Letters*, *31*(7), 8–11. doi: 10.1029/2004GL019491

Shapiro, N. M., Campillo, M., Stehly, L., & Ritzwoller, M. H. (2005). High-resolution surface-wave tomography from ambient seismic noise. *Science*, *307*(5715), 1615–1618. doi: 10.1126/science.1108339

Snieder, R., & Wapenaar, K. (2010). Imaging with ambient noise. *Physics Today*, *63*(9), 44–49. doi: 10.1063/1.3490500

Stutzmann, E., Ardhuin, F., Schimmel, M., Mangeney, A., & Patau, G. (2012). Modelling long-term seismic noise in various environments. *Geophysical Journal International*, *191*(2), 707–722. doi: 10.1111/j.1365-246X.2012.05638.x

Sánchez-Sesma, F. J., & Campillo, M. (2006). Retrieval of the Green's function from cross correlation: The canonical elastic problem. *Bulletin of the Seismological Society of America*, *96*(3), 1182–1191. doi: 10.1785/0120050181

Teodor, D., Comina, C., Khosro Anjom, F., Brossier, R., Valentina Socco, L., & Virieux, J. (2021, July). Challenges in shallow target reconstruction by 3D elastic full-waveform inversion — Which initial model? *GEOPHYSICS*, *86*(4), R433–R446. Retrieved 2022-06-17, from https://library.seg.org/doi/full/10.1190/geo2019-0523.1 doi: 10.1190/geo2019-0523.1

Tolman, H. L., & Chalikov, D. (1996). Source terms in a third-generation wind wave model. *Journal of Physical Oceanography*, *26*(11), 2497–2518. doi: 10.1175/1520-0485(1996)026⟨2497:STIATG⟩2.0.CO;2

Tromp, J., Luo, Y., Hanasoge, S., & Peter, D. (2010). Noise cross-correlation sensitivity kernels. *Geophysical Journal International*, *183*(2), 791–819. doi: 10.1111/j.1365-246X.2010.04721.x

Tsai, V. C., & Sager, K. (2022). The relationship between cross correlations and Green's functions in ambient noise interferometry with Bayesian constraints. *Geophysical Journal International*, *228*(2), 816–825. doi: 10.1093/gji/ggab376

Umlauft, J., Lindner, F., Roux, P., Mikesell, T. D., Haney, M. M., Korn, M., & Walter, F. T. (2021). Stick-Slip Tremor Beneath an Alpine Glacier. *Geophysical Research Letters*, *48*(2), 1–10. doi: 10.1029/2020GL090528

van Driel, M., Krischer, L., Stähler, S., Hosseini, K., & Nissen-Meyer, T. (2015). Instaseis: Instant global seismograms based on a broadband waveform database. *Solid Earth*, *6*(2), 701–717.

Virieux, J., & Operto, S. (2009, November). An overview of full-waveform inversion in exploration geophysics. *GEOPHYSICS*, *74*(6), WCC1–WCC26. Retrieved 2022-06-17, from https://library.seg.org/doi/full/10.1190/1.3238367 doi: 10.1190/1.3238367

Wapenaar, K. (2004). Retrieving the elastodynamic Green's function of an arbitrary inhomogeneous medium by cross correlation. *Physical Review Letters*, *93*(25), 1–4. doi: 10.1103/PhysRevLett.93.254301

Wapenaar, K., & Fokkema, J. (2006). Green's function representations for seismic interferometry. *Geophysics*, *71*(4), SI33–SI46. doi: 10.1190/1.2213955

WAVEWATCH III. (2005, October). Retrieved 2022-07-04, from https://polar.ncep.noaa.gov/waves/wavewatch/

Weaver, R., Froment, B., & Campillo, M. (2009). On the correlation of non-isotropically distributed ballistic scalar diffuse waves. *The Journal of the Acoustical Society of America*, *126*(4), 1817. doi: 10.1121/1.3203359

Woodard, M. F. (1997). Implications of Localized, Acoustic Absorption for Heliotomographic Analysis of Sunspots. *The Astrophysical Journal*, *485*(2), 890–894. doi: 10.1086/304468

Xu, Z., Dylan Mikesell, T., Gribler, G., & Mordret, A. (2019). Rayleigh-wave multicomponent cross-correlation-based source strength distribution inversion. Part 1: Theory and numerical examples. *Geophysical Journal International*, *218*(3), 1761–1780. doi: 10.1093/gji/ggz261

Xu, Z., & Mikesell, T. D. (2022). Estimation of Resolution and Covariance of Ambient Seismic Source Distributions: Full Waveform Inversion and Matched Field Processing. *Journal of Geophysical Research: Solid Earth*, *127*(6), e2022JB024374. Retrieved 2022-06-15, from https://onlinelibrary.wiley.com/doi/abs/10.1029/2022JB024374 doi: 10.1029/2022JB024374

Zhan, Z., Tsai, V. C., & Clayton, R. W. (2013). Spurious velocity changes caused by temporal variations in ambient noise frequency content. *Geophysical Journal International*, *194*(3), 1574–1581. doi: 10.1093/gji/ggt170